Toroidal asymmetry of 2-D divertor heat flux profiles during the ELM and 3-D field application in NSTX

J-W. Ahn[1], K.F. Gan[2], F. Scotti[3], R. Maingi[1], J.M. Canik[1], T.K. Gray[1], J.D. Lore[1], A.G. McLean[4], A.L. Roquemore[3], and V.A. Soukhanovskii[4]

[1]Oak Ridge National Laboratory, Oak Ridge, TN 37831, USA

[2]Institute of Plasma Physics, Chinese Academy of Sciences, Hefei, China

[3]Princeton Plasma Physics Laboratory, Princeton, NJ 08543, USA

[4]Lawrence Livermore National Laboratory, Livermore, CA 94551, USA

E-mail: jahn@pppl.gov

Abstract. A set of 2-D heat flux profiles with high temporal resolution have been obtained using a novel heat conduction code, TACO, for naturally ELMy and 3-D field applied H-mode plasmas in NSTX. A new analysis technique has enabled quantitative measurement of the 'degree of asymmetry (DoA)' in both the peak heat flux (q_{peak}) and heat flux width (λ_q) as well as the 2-D average value for both quantities, representing the whole 2-D plane observed by the IR camera diagnostics at each time slice. The 2-D averages for q_{peak} and λ_q revealed that heat flux width increases or decreases during the ELM, depending on the ELM type, and decreases with increasing peak heat flux for ELM peak times. The temporal variation of the asymmetry in q_{peak} and λ_q for several types of ELMs has been investigated and it is found that each asymmetry, as well as the correlation between each other, reaches a maximum at ELM peak times and becomes lower later in the ELM cycle. Asymmetry in q_{peak} at ELM peak times is usually higher than that in λ_q by a factor of 2-3 (in term of the magnitude of DoA) for all ELM types, except for type-V ELMs where both asymmetries are similar. This indicates that type-V ELMs produce relatively higher asymmetry in heat flux width than other types of ELMs. The asymmetry in λ_q for type-V ELMs as a function of heat flux width and peak heat flux is indeed located separately from the combined trend of all other types of ELMs. Both asymmetries in q_{peak} and λ_q are a strong function of peak heat flux, *i.e*. high peak heat flux leads to high asymmetry. On the other hand, the asymmetries are only weakly affected by the mid-plane heat flux width ($\lambda_{q,mid}$) except at lower $\lambda_{q,mid}$ values, *eg* near $\lambda_{q,mid}$~2cm for the dataset studied in this work, where both asymmetries are inversely related to $\lambda_{q,mid}$ very strongly. ELMs triggered by the applied n=3 magnetic perturbation fields are compared with naturally occurring type-I ELMs. It is found that both asymmetries at ELM peak times for triggered ELMs increase more slowly with increasing q_{peak} than for type-I ELMs, but the increase in the λ_q asymmetry is even slower. This also leads to a significantly weaker correlation between the two asymmetries than the case for type-I ELMs. The underlying physical mechanisms for the observed dynamics of divertor heat flux asymmetry are not yet understood and more detailed study is necessary for the effect of 3-D field application and ELMs on the temporal and spatial distribution of divertor heat flux.

1. Introduction

Asymmetric divertor heat fluxes have recently drawn significant attention in various fusion studies, such as external application of 3-D magnetic perturbations [1,2,3,4] and naturally-occurring edge localized modes (ELMs) [5]. A slight breaking of axisymmetry in the magnetic topology, either internally arisen or externally induced by applied 3-D fields, leads to complex physical phenomena, including the suppression/mitigation of ELMs and the modification of divertor flux profiles. Understanding the behavior of asymmetric divertor heat flux deposition, both steady state and transient, and its underlying physics in various plasma conditions is of practical importance for future machines because the design and engineering constraints on plasma facing components (PFC) are usually based on the assumption of axisymmetric fluxes.

This is even more critical for the spherical tokamak (ST), because its compact size can make heat flux management even more challenging than in higher aspect ratio tokamaks. The divertor toroidal asymmetry directly reflects the respective asymmetric physical process upstream, and therefore can also provide useful information for the investigation of pedestal physics.

The use of a 2-D infrared (IR) camera plays a vital role in obtaining surface temperature data and for the derivation of heat flux profiles. The primary caveat in the study of asymmetric heat flux profiles is that divertor heat conduction codes, such as THEODOR [6], are usually in 2-D, *i.e.* 1-D in the direction of the tile depth, and 1-D along the radial extent of the plasma facing surface. The obtained heat flux profile is therefore only 1-D, *i.e.* in the radial direction (r) chosen at a particular toroidal location (Φ). This significantly restricts the capability of investigating toroidal asymmetry in the divertor heat flux profiles. We have recently implemented a novel heat conduction code, TACO [7], in National Spherical Torus eXperiment (NSTX) to obtain 2-D heat flux profiles including the upgrade to incorporate thin surface layers that naturally form on PFCs [8].

2. Experimental setup

Experiments were conducted in various types of ELMy H-mode plasmas, *i.e.* type-I, III, and V, and the 3-D field application was made to a series of lithium enhanced ELM-free plasmas. The toroidal magnetic field (B_t) at the magnetic axis was fixed at ~0.4 T, and the neutral beam injected power (P_{NBI}) of 2.5-6 MW was used. Plasmas were highly shaped (elongation κ ~ 2.0-2.4, triangularity δ ~ 0.5-0.8), and the plasma current was 600-800 kA. The equilibrium was maintained as a lower single-null with the direction of the *B*-field such that the ion ∇B drift moves towards the primary X-point. 3-D field pulses in NSTX are applied using a mid-plane coil set. In the experiments discussed here, these coils were configured to apply n=3 perturbative magnetic fields and the coil current was sufficiently high ($I_{3\text{-}D}$ = 0.75 - 1 kA) to trigger ELMs, resulting in $\delta B/B$ ~ 0.1 % for the integrated δB over the coil surface. The PFC surface temperature is measured with an SBF-161 IR camera [9], covering toroidal angle Φ ~ 110- 160^o for the full frame size with a temporal resolution of 1.6 to 6.3 kHz (depending on the frame size). This is used to calculate 2-D heat flux profiles by TACO and the obtained 2-D heat flux data are readily remapped to the (r, Φ) plane, which is necessary for the analysis of asymmetric heat flux profiles. Figure 1 is an example of such 2-D heat flux profiles for an inter-ELM and ELM peak time.

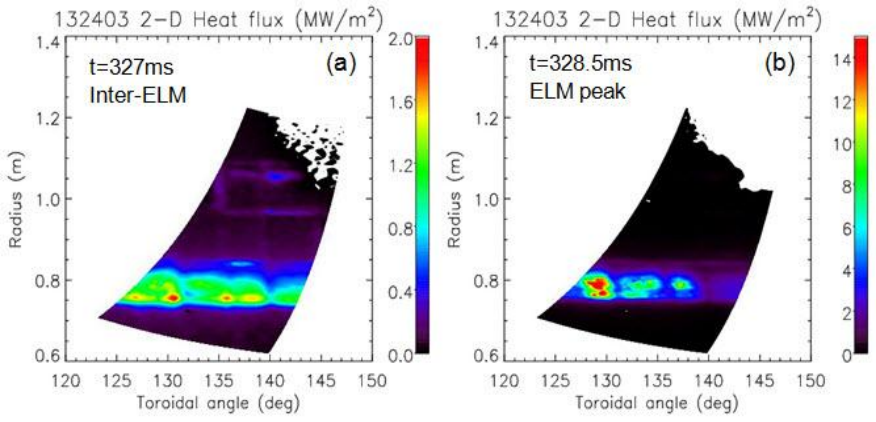

FIG. 1 Images of 2-D lower divertor heat flux profiles in NSTX for a type-III ELMy plasma, remapped from (x, y) to the (r, Φ) plane. (a) is during the inter-ELM period and (b) is at an ELM peak time.

3. Analysis of asymmetric divertor heat flux for naturally occurring ELMs

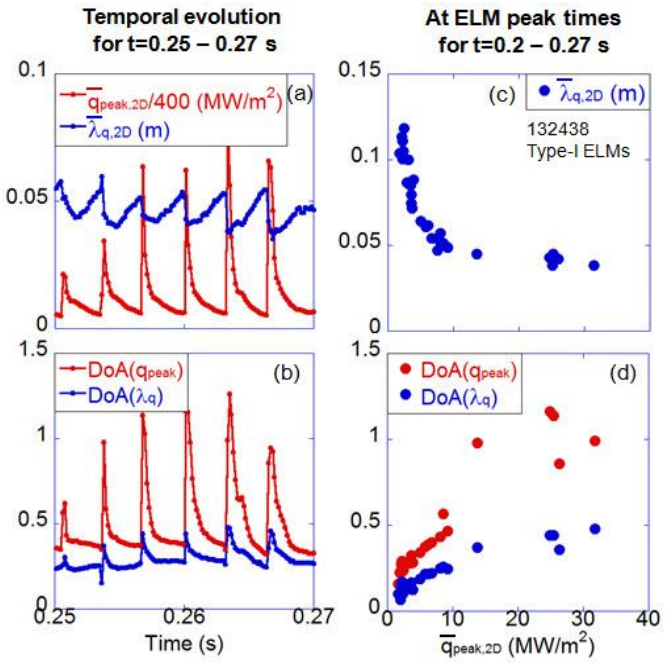

FIG. 2 Temporal evolution of 2-D average peak heat flux and heat flux width (a) during a type-I ELMy H-mode, and of the degree of asymmetry (DoA) for q_{peak} and λ_q (b). Plot (c) shows the relation between the 2-D average peak heat flux and average heat flux width at ELM peak times, and (d) shows the relation between the two DoAs and the 2-D average q_{peak}. This result is for type-I ELMs.

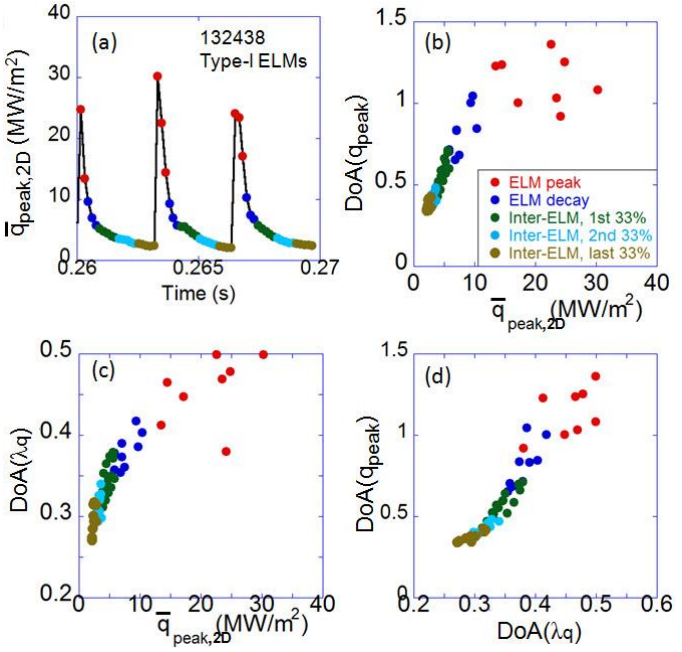

FIG. 3 (a) Temporal evolution of 2-D average peak heat flux during a type-I ELMy H-mode. DoA(q_{peak}) and DoA(λ_q) as a function of average q_{peak} ((b) and (c), respectively). Relation between DoA(λ_q) and DoA(q_{peak}) is shown in (d). DoA(q_{peak}) and DoA(λ_q) are defined for the whole 2-D plane at each time slice. Data are color coded according to the ELM cycle.

3.1 TACO heat conduction code for 2-D heat flux profile

TACO has been implemented for use on NSTX to calculate heat flux at the divertor surface for the 2-D data observed by the IR camera. This provides a significant advantage over 1-D radial profiles, as it allows the study of toroidal distribution of heat deposition. We also incorporated the thin surface film correction applied in THEODOR [6] into the process of solving the heat conduction equation [8]. A heat transmission coefficient, α, of 40 - 60 $kWm^{-2}K^{-1}$ was found to best account for poor surface layer adhesion to the tile substrate. This value was used for all analysis presented in this paper. The re-mapping of heat flux data to r and Φ allowed for the evaluation of peak heat flux q_{peak} and heat flux width λ_q for each toroidal angle, which in turn generates a toroidal array of these quantities at each time slice. Here, we used the definition of integral λ_q used in [10], *i.e.* $\lambda_q = P_{div} / \left(2\pi r_{peak}^{div} q_{peak}^{div}\right)$.

3.2 Toroidal asymmetries in peak heat flux and heat flux width for type-I ELMs

In order to quantify how asymmetric the toroidal distribution of q_{peak} and λ_q is, the toroidal degree of asymmetry (DoA) for q_{peak} and λ_q, representing the whole 2-D plane monitored by the IR camera, as a function of time was defined as $DoA(q_{peak}) = \sum\left(\sigma_{qpeak} / \bar{q}_{peak}\right) / N$ and $DoA(\lambda_q) = \sum\left(\sigma_{\lambda q} / \bar{\lambda}_q\right) / N$. Here, σ_{qpeak} and $\sigma_{\lambda q}$ are the standard deviation of q_{peak} and λ_q over data in a toroidal array and N is the total number of toroidal arrays. $\bar{q}_{peak}$ and $\bar{\lambda}_q$ are the average over values in each toroidal array. Therefore,

the standard deviation is normalized by a mean value of q_{peak} and λ_q respectively in each toroidal array before being averaged for the whole 2-D plane to finally produce a DoA value at each time slice. In case of ELMs, the helical heat deposition produces strong toroidal asymmetry for both q_{peak} and λ_q and thus generates additional scatter of data around the mean value to the background scatter level. An example of temporal evolution of $\bar{q}_{peak}$ and $\bar{\lambda}_q$ for a type-I ELMy discharge is given in figure 2(a). Note that an average value representing the 2-D plane for each of q_{peak} and λ_q is introduced and denoted as $\bar{\lambda}_{q,2D}$ and $\bar{q}_{peak,2D}$. It is seen that $\bar{\lambda}_{q,2D}$ drops during the ELM rise time while $\bar{q}_{peak,2D}$ jumps. Although the decrease of λ_q during the ELM is opposite to the modest ELM broadening of heat flux width reported from some other machines [11], the deposited ELM power rapidly increases and peaks at the same time as that for the peak heat flux. Figure 2(b) shows the temporal evolution of DoA for both q_{peak} and λ_q and it is shown that both asymmetries rapidly increase with the rise of peak heat flux. It is interesting to note that DoA(λ_q) increases during the ELM rise time even though λ_q itself decreases. Probing dependence of parameters on the 2-D average of peak heat flux at ELM peak times revealed that heat flux width decreases with increasing peak heat flux (see figure 2(c)). On the other hand, DoA for both q_{peak} and λ_q increase with increasing q_{peak} (figure 2(d)). The absolute value of DoA(q_{peak}) is always greater than DoA(λ_q) and the ratio DoA(q_{peak})/DoA(λ_q) is typically ~2-3. The dependence of DoA dynamics on the ELM cycle was also investigated. Figure 3 shows the result for the same discharge as in figure 2, color-coded during the ELM cycle, across several ELMs. It is found that both DoA(q_{peak}) and DoA(λ_q) become largest at the ELM peak times and DoA(q_{peak}) can be as high as ~1.4 while DoA(λ_q) can reach up to ~0.5 for the dataset examined in this work. Both DoA values increase with increasing q_{peak} and therefore the degree of asymmetric heat deposition is highest at the ELM peak times, while it becomes lower toward the later stage of the inter-ELM period (see figures 3(b) and 3(c)). This dependence of the degree of asymmetric heat deposition on the ELM cycle is also related to the absolute value of peak heat flux; higher peak heat flux leads to higher degree of asymmetric q_{peak} and λ_q. It is also found from figure 3(d) that the correlation between DoA(q_{peak}) and DoA(λ_q) is the strongest at the ELM peak times and becomes weaker later in the ELM cycle.

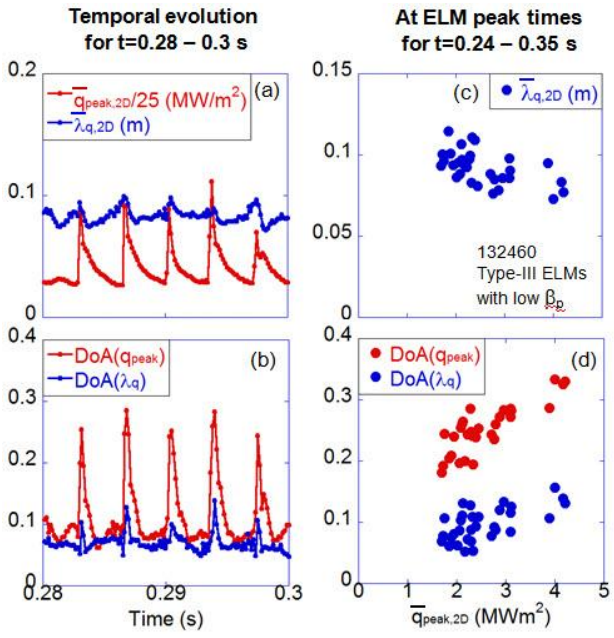

FIG. 4 Temporal evolution of 2-D average peak heat flux and heat flux width (a) for type-III ELMs with low β_p, and of the degree of asymmetry (DoA) for q_{peak} and λ_q (b). Plot (c) shows the relation between 2-D average peak heat flux and average heat flux width at ELM peak times, and (d) shows the relation between the two DoAs and the 2-D average q_{peak}.

3.3 Toroidal asymmetries for type-III and type-V ELMs

Type-III ELMs in NSTX are found to have different characteristics with different pedestal performance [12]. Although the specific pedestal parameter as an indicator of the pedestal performance is yet to be identified, it is found that the poloidal beta (β_p) is a good quantity to differentiate different ELM characteristics from each other. For type-

III ELMs with high β_p (≥ 0.5) the temporal behaviour of $\bar{q}_{peak,2D}$ and $\bar{\lambda}_{q,2D}$ is similar to that of type-I ELMs. However, for type-III ELMs with low β_p (≤ 0.5), $\bar{\lambda}_{q,2D}$ for an individual ELM increases during the ELM rise time, which is opposite to the behaviour for type-I ELMs, see figure 4(a). Interestingly, $\bar{\lambda}_{q,2D}$ at ELM peak times for multiple ELMs still decreases with increasing peak heat flux, see figure 4(c). The general trend of DoA(q_{peak}) and DoA(λ_q) as a function of $\bar{q}_{peak,2D}$ is similar to the one for type-I ELMs irrespective of high or low β_p, see figures 4(b) and 4(d).

Type-V ELMs are a small ELM regime [13] identified in NSTX and have a single or double filamentary structure that originates usually in the lower part of the H-mode pedestal where T_e < 150 eV. The temporal behavior of $\bar{q}_{peak,2D}$ and $\bar{\lambda}_{q,2D}$ for type-V ELMs shows a similar trend to that of low β_p type-III ELMs, although the ELM size is significantly smaller by several factors; an individual type-V ELM increases both the absolute value and DoA of peak heat flux and heat flux width. One thing to note is that the two DoAs values are usually comparable with each other for type-V ELMs, different from the consistently higher DoA(q_{peak}) than DoA(λ_q) by a factor of ~2-3 for all other ELM types. This is primarily due to the fact that DoA(q_{peak}) values for type-V ELMs are normally smaller than those for low β_p type-III ELMs, while DoA(λ_q) is similar for both cases. That is, type-V ELMs have relatively higher DoA(λ_q) than other types of ELMs. A more comprehensive comparison between different ELM types will be made in section 3.4. Generally, the absolute values of both DoAs tend to scale with the ELM size for each type of ELM.

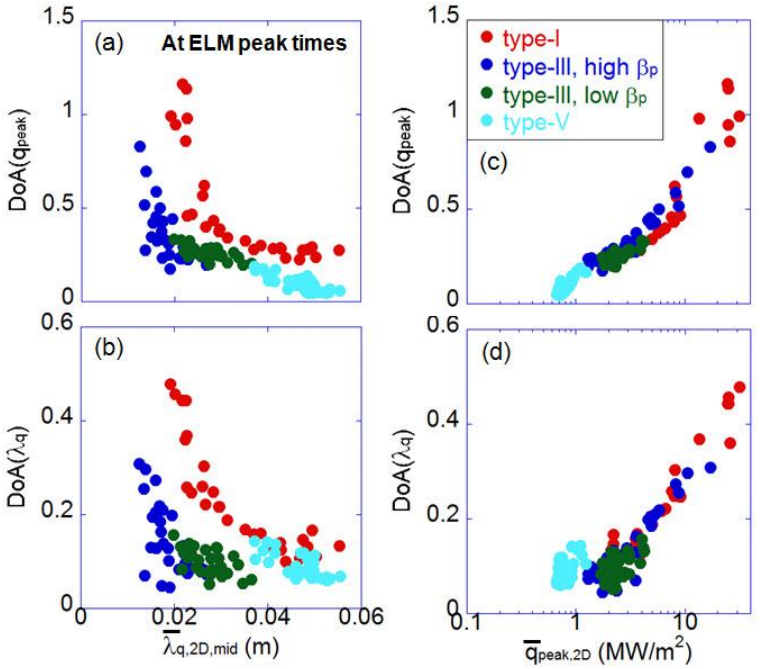

FIG. 5 DoA(q_{peak}) and DoA(λ_q) at ELM peak times as a function mid-plane heat flux width, (a) and (b) respectively, and as a function of peak heat flux, (c) and (d), for all types of ELMs studied in this work.

3.4 Comparison between type-I, III, and V ELMs

We now compare the two DoAs as a function of peak heat flux and heat flux width for all ELM types (type-I, type-III with high and low β_p, and type-V). In order to do this, we use the mid-plane heat flux width ($\bar{\lambda}_{q,2D,mid}$), which takes account of the flux expansion between the mid-plane and the divertor surface for $\bar{\lambda}_{q,2D}$. In figures 5(a) and 5(b), it can be seen that both DoAs rapidly decrease with increasing $\bar{\lambda}_{q,2D,mid}$ for low $\bar{\lambda}_{q,2D,mid}$ ($\leq$ 2–2.5 cm) values, but then the rate of decrease significantly slows or saturates for $\bar{\lambda}_{q,2D,mid}$ higher than 2–2.5 cm. On the other hand, both DoAs increase with increasing $\bar{q}_{peak,2D}$ for all ELM types with the

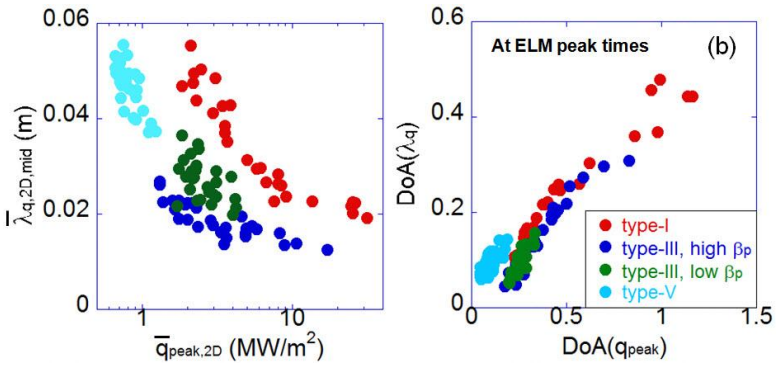

FIG. 6 (a) Relation between 2-D average heat flux width and peak heat flux, and (b) relation between DoA(q_{peak}) and DoA(λ_q), for all ELM types.

rate of increase slowing for higher heat flux values (figures 5(c) and 5(d), with the x-axis in the log scale). Another thing to note is that DoA(λ_q) values for type-V ELMs are located discretely, *i.e.* higher than the scaled values, from the trend of all other ELM types (see figure 5(d)), while DoA(q_{peak}) data follow the trend through all types of ELMs. This relative increase of DoA(λ_q) leads to the ratio of DoA(q_{peak})/DoA(λ_q) close to 1. Figure 6 is another comparison of $\bar{q}_{peak,2D}$ *vs* $\bar{\lambda}_{q,2D,mid}$ and DoA(q_{peak}) *vs* DoA(λ_q) at ELM peak times for all ELM types. The observed trend of inverse relationship between heat flux width and peak heat flux is not beneficial for the extrapolation to the future machine, see figure 6(a). Out of all four types of ELMs, type-V ELMs exhibit the most desired characteristics, *i.e.* the lowest peak heat flux and the largest heat flux width. Unlike figure 6(a), the two degrees of asymmetry are found to have positive dependence on each other in figure 6(b). Also, data for type-I and III ELMs overlap to form a significant trend, keeping the ratio of DoA(q_{peak})/DoA(λ_q) ~ 2–2.5, but type-V ELMs are located separately because of the reduced value of ratio with ~1. Another parameter of interest regarding the ELM heat flux is the total power that is deposited by an ELM and its dependence on the 2-D average peak heat flux and heat flux width. Figure 7 shows the result and basically the ELM power increases almost exponentially with increasing peak heat flux with data for all ELM types forming a consistent trend. On the other hand, the dependence of power on the mid-plane heat flux width is rather flat for a significant portion of the whole range of heat flux width, except that data for type-I and III ELMs show a very strong negative dependence at low $\bar{\lambda}_{q,2D,mid}$ (~2 cm). Also, ELM power for type-I ELMs is noticeably higher than for other ELM types for a similar level of $\bar{\lambda}_{q,2D,mid}$.

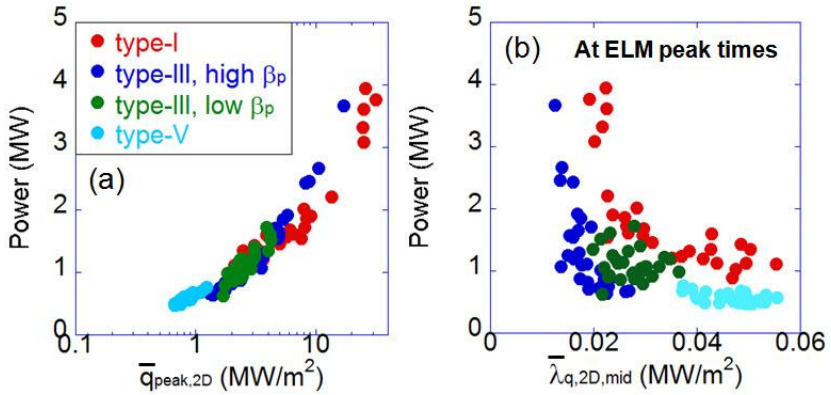

FIG. 7 Dependence of ELM power on 2-D average peak heat flux (a) and mid-plane heat flux width (b) for all ELM types.

4. Toroidal asymmetries for ELMs triggered by applied 3-D fields

The application of external 3-D fields is found to trigger ELMs in the lithium enhanced ELM-free H-mode plasmas in NSTX [14]. The triggered ELMs are large and the exact triggering mechanism is not fully understood yet. It is therefore important to examine characteristics of

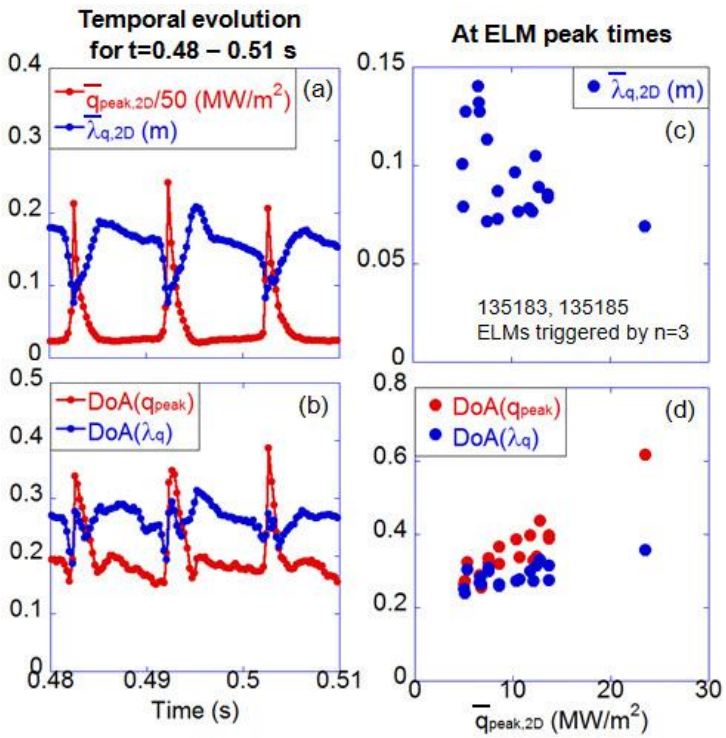

FIG. 8 Temporal evolution of 2-D average peak heat flux and heat flux width (a) for the ELMs triggered by n=3 magnetic perturbation, and of the degree of asymmetry (DoA) for q_{peak} and λ_q (b). Plot (c) shows the 2-D average heat flux width as a function of average peak heat flux at ELM peak times, and (d) shows the dependence of the two DoAs on the average q_{peak}.

2-D heat flux deposition for these ELMs and compare it with those for naturally occurring ELMs. Figure 8(a) shows the temporal evolution of $\bar{q}_{peak,2D}$ and $\bar{\lambda}_{q,2D}$ and 8(b) is the evolution of DoA for these two parameters. The heat flux width drops significantly during the ELM rise time and quickly recovers during the ELM decay period, but it continues to decrease slowly for the remainder of each inter-ELM period. This is an important difference from the naturally occurring ELMs, where $\bar{\lambda}_{q,2D}$ increases during the inter-ELM period for all types of ELM while it can either drop or rise during the ELM rise period depending on the ELM type (see sections 3.2 and 3.3). As for the change in the degree of asymmetry, it is noted that DoA(λ_q) suddenly drops immediately before the peak heat flux begins to increase due to the ELM burst, and then rises during the ELM rise time (see figure 8(a)). However, the increase of DoA(λ_q) is not prominent compared to the background level during the inter-ELM period, while DoA(q_{peak}) shows a clear spike for each ELM (figure 8(b)). This is also reflected in the data for ELM peak times, see figure 8(d) where DoA(λ_q) only shows a very weak positive dependence on the peak heat flux while the dependence of DoA(q_{peak}) becomes stronger with higher q_{peak}. An inverse relation between $\bar{\lambda}_{q,2D}$ and $\bar{q}_{peak,2D}$ is also observed in figure 8(c) but the scatter level is significantly higher than the cases for naturally occurring ELMs (figures 2(c) and 4(c)).

We have compared the general trends for the triggered ELMs with those for type-I ELMs at ELM peak times, and the results are presented in figure 9. Both for DoA(q_{peak}) and DoA(λ_q),

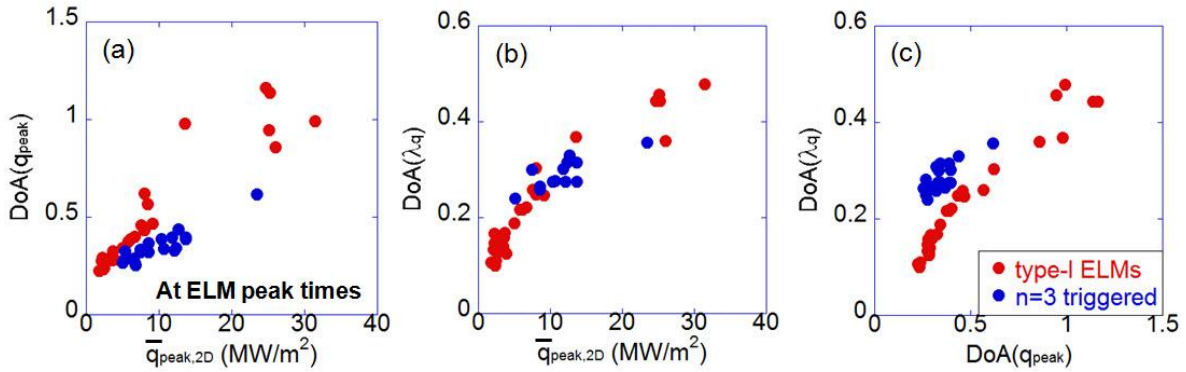

FIG. 9 Dependence of DoA(q_{peak}) and DoA(λ_q) on the 2-D average peak heat flux, (a) and (b) respectively, and the relation between the two DoAs with each other. Note that these are at ELM peak times and data for type-I ELMs (red) and ELMs triggered by n=3 fields (blue) are compared in each case.

the dependence on peak heat flux is noticeably weaker for the triggered ELMs (see figures 9(a) and 9(b)). Figure 9(c) shows relation between the two DoAs and it is seen that variation of DoA(λ_q) is significantly weaker than that of DoA(q_{peak}). Although we do not have a physics ground to explain this observation yet, this result may provide an interesting insight into the ELM triggering by the applied 3-D fields. For example, the weak variation of DoA(λ_q) might be related to the observed 'phase lock' of heat flux profile during the ELM to the applied 3-D field structure reported in [15,16], while the naturally occurring ELMs would undergo nonlinear MHD processes that may result in higher toroidal asymmetry in both the peak heat flux and heat flux width. This needs more detailed study to elucidate the underlying physics.

Acknowledgements

This work was supported by the US Department of Energy, contract numbers DE-AC05-000R22725, DE-AC52-07NA27344, and DE-AC02-09CH11466.

References

[1] SCHMITZ, O., EVANS, T.E., FENSTERMACHER, M.E., et al., Plasma Phys. Control. Fusion **50** (2008) 124029

[2] JAKUBOWSKI, M.W., EVANS, T.E., FENSTERMACHER, M.E., et al., Nucl. Fusion **49** (2009) 095013

[3] AHN, J-W., CANIK, J.M., SOUKHANOVSKII, V.A., et al. Nucl. Fusion **50** (2010) 045010

[4] AHN, J-W., MAINGI, R., CANIK, J.M., et al., Phys. Plasmas **18** (2011) 056108

[5] EICH, T., HERRMANN, A., NEUHAUSER, J., et al., Plasma Phys. Control. Fusion **47** (2005) 815

[6] HERRMANN, A., JUNKER, W., GUNTHER, K., et al., Plasma Phys. Control. Fusion **37** (1995) 17

[7] CASTLE, G., "Theory and Operating Instructions for the taco_run code", COMPASS Note 97.16, UKAEA Fusion (1997)

[8] GAN, K.F., et al., "2D divertor heat flux distribution using a 3-D heat conduction solver in NSTX", submitted to Rev. Sci. Instrum.

[9] AHN J-W., MAINGI R., MASTROVITO D. and ROQUEMORE A.L., Rev. Sci. Instrum. **81** (2010) 023501

[10] LOARTE, A., BOSCH, S., CHANKIN, A., et al., J. Nucl. Mater. **266-269** (1999) 587

[11] HERRMANN, A., EICH, T., JACHMICH, S., et al., J. Nucl. Mater. **313-316** (2003) 759

[12] GAN, K.F., et al., "Comparison of heat flux profile evolution during different types of edge localized modes in the National Spherical Torus Experiment", submitted to Nucl. Fusion

[13] MAINGI, R., et al., Nucl. Fusion **45** (2005) 264

[14] CANIK, J.M., et al., Phys. Rev. Lett. **104** (2010) 045001

[15] AHN, J-W., et al., J. Nucl. Mater. **415** (2011) S918

[16] AHN, J-W., et al., submitted to Plasma Phys. Control. Fusion